Letter

Turbulence in disguise: Reactive flows in porous media mimic turbulent behavior

Emeric Boigné [1,*], Sadaf Sobhani [2], Joseph C. Ferguson [1], and Matthias Ihme [1,3]
[1]*Department of Mechanical Engineering, Stanford University, Stanford, California 94305, USA*
[2]*Sibley School of Mechanical and Aerospace Engineering, Cornell University, Ithaca, New York 14853, USA*
[3]*Department of Photon Science, SLAC National Accelerator Laboratory, Menlo Park, California 94025, USA*

(Received 18 May 2024; revised 4 July 2024; accepted 26 September 2024; published 21 October 2024)

Chemical reactions in porous media play a pivotal role in various biological, environmental, and engineering applications, yet understanding flow-chemistry coupling within pores remains an outstanding challenge. This article examines a parallel between how chemical reaction fronts are impacted by (i) turbulence in unconfined flows, and (ii) hydrodynamic dispersion in porous media flows, even at laminar flow conditions. A regime diagram is constructed from which hitherto overlooked regime transitions are identified. The results are expected to improve our understanding of pore-scale coupling, with implications relevant to a broad range of applications.

DOI: 10.1103/PhysRevFluids.9.L101201

Introduction. Flows of chemically reactive mixtures in porous media are of fundamental importance to a wide range of engineering systems, as well as biological and environmental applications, which include clean energy technologies [1], biofuel reactors [2,3], power generation [4], and filtration combustion [5,6]. These flows are primarily governed by the physical coupling occurring at the pore scale between hydrodynamic dispersion and chemistry, especially when reaction fronts propagate fast enough to neglect the interphase heat exchange [7,8].

In porous media flows, momentum exchange governs the dispersion, which itself controls the transport and mixing of chemical species [9]. With increasing velocity, the flow transitions from laminar to inertial steady conditions, before evolving into unsteady and turbulent conditions, which are characterized by the integral velocity fluctuations u_l and integral length-scale l. For nonreactive flows, the Reynolds number is sufficient to describe these flow regimes, where it is defined at the pore scale as $\mathrm{Re}_p = U_p D/\nu$, with D the characteristic pore size, ν the kinematic viscosity, and U_p the interstitial flow velocity related to the Darcy velocity U_D via $U_p = U_D/\varepsilon$, with ε the porosity [10].

In reactive flows, the chemistry introduces another set of physical parameters critical to the flow regime: the chemical length scale δ_c and laminar reaction speed S_L [11–13], with a corresponding time scale $\tau_c = \delta_c/S_L$ and Damköhler number $\mathrm{Da} = \tau_l/\tau_c = (S_L/u_l)(l/\delta_f)$. For unconfined turbulence, a transition is known to occur from a regime of weak turbulence-chemistry interaction to a regime of strong coupling as the Karlovitz number, Ka, exceeds unity [14,15], where Ka is defined as $\mathrm{Ka} = \tau_c/\tau_\eta$, with $\tau_\eta = l_\eta/U_\eta$ being the turnover time of the smallest flow scales of size l_η and velocity U_η.

Despite a detailed understanding of both hydrodynamic dispersion, and turbulence-chemistry interaction, we still lack a unified theory to describe the regimes of reactive flows through porous media. As a result, despite the many experimental and computational studies investigating these

*Contact author: eboigne@stanford.edu

flows, the regimes of flow-chemistry interaction are rarely characterized, and critical transitions are often overlooked. In particular, while experimental evidence indicates the importance of unsteady dynamics of reaction fronts [16], their propagation at Reynolds numbers exceeding 900 is still analyzed under the hypothesis of laminar flow-chemistry interaction [17].

This article addresses this issue by analyzing the fundamental pore-scale interaction between dispersion and chemistry across a wide range of coupling regimes. Specifically, by combining theoretical analysis, previously published experimental data, and new numerical simulations, we show that hydrodynamic dispersion impacts reaction fronts similarly to turbulence in free flows, even at nominally laminar flow conditions. While this parallel was first hypothesized from a purely theoretical perspective [18], so far only a few flow conditions were interpreted in light of turbulent combustion regimes [12]. Here, we explore the underlying coupling over a broad range of inertial and chemical conditions, with Re_p varying from 20 to 2120 and D/δ_c from 0.67 to 5.3. In particular, the reaction front wrinkles in the Darcy flow regime ($\mathrm{Re}_p \lesssim 50$) [4,19–21], and in creeping flows ($\mathrm{Re}_p \lesssim 5$), the interstitial velocities can be described by Gaussian or exponential distributions [22]. Our analysis focuses on the inertial flow regimes most relevant to practical applications ($\mathrm{Re}_p \gtrsim 50$), where flows feature unsteady vortex shedding, jet impinging, and intermittent turbulence [5,8,11,13,16,17,23–25]. From extensive parametric variations, we identify a transition in the flow-chemistry coupling and fundamental scaling laws that hold true across regimes. Building upon these findings, we propose a regime classification for reactive flows in porous media that integrates the established regimes of both inertial flows in porous media and turbulence-chemistry interactions in unconfined flows.

Method. We perform detailed pore-resolved simulations of a reactive mixture flowing within 2D arrays of adiabatic cylinders with diameter D and constant porosity $\varepsilon = 0.7$. The focus on 2D flows enables a comprehensive analysis across multiple physical regimes, whereas 3D simulations remain limited to a few operating conditions [8,11,17,24,26,27]. Imposing adiabatic wall boundary conditions isolates the hydrodynamic interaction from the conjugate heat transfer that can lead to superadiabatic conditions [11], ignition-assisted propagation [13], and thermal quenching and instabilities [16,17].

Twenty-one numerical calculations of reactive flows are performed by solving the fully compressible reactive Navier-Stokes equations with a mixture of methane and air considering a one-step reaction $CH_4 + 2O_2 \rightarrow CO_2 + 2H_2O$, which is chosen to represent a general chemical reaction front. The multispecies transport equations are discretized using an unstructured finite-volume scheme, with a transport equation accounting for differential diffusion with a mixture-averaged diffusivity for each species [28]. The Knudsen number is below 0.001, and only continuum mechanics is considered.

The chemical kinetics are described with a single-step Arrhenius equation with a forward reaction rate in mol/(m^3 s) equal to $k_f = [X_{\mathrm{CH_4}}][X_{\mathrm{O_2}}]^{1/2} A \exp\{-E_a/RT\}$, where $[X_{\mathrm{CH_4}}]$ and $[X_{\mathrm{O_2}}]$ are the molar concentrations of CH_4 and O_2, $E_a = 20$ kcal/mol is the activation energy, and $A = 1.1 \times 10^{10}$ cm$^{3/2}$ mol$^{-1/2}$ s^{-1} is the pre-exponential factor [29]. The mixture equivalence ratio is fixed at $\phi = 0.7$, which yields $S_L = 0.23$ m/s and $\delta_c = 0.6$ mm. The reaction zone thickness δ_c is evaluated from the thermal zone thickness, defined as the ratio $\delta_c = \Delta T/\max(\mathrm{d}T/\mathrm{d}x)$ of the change in temperature ΔT through the reaction to the maximum temperature gradient across a 1D reaction front.

The porous media of 8 cm long is made of randomly placed cylinders. The cylinder array is located 2.5 cm away from the inlet and outlet of the domain simulated, which is a rectangle of 13 cm × 2 cm. The reaction front is identified by extracting isocontours of a progress variable with a value of $C = 0.85$, defined from the mass fraction Y_F of fuel as $C = 1 - Y_F/Y_{F,u}$, where $Y_{F,u}$ is the unreacted mass fraction of CH_4 at the inlet [30]. Further details on the simulations are provided in the Supplemental Material [31] and in previous work [32,33].

Pore-scale coupling processes. The primary impact of the porous media on the flow is to introduce a no-slip condition at the fluid-solid interface, which results in shear, dispersion, and heterogeneous distribution of kinetic energy within the pores [22,34]. In 2D, there is no vortex-

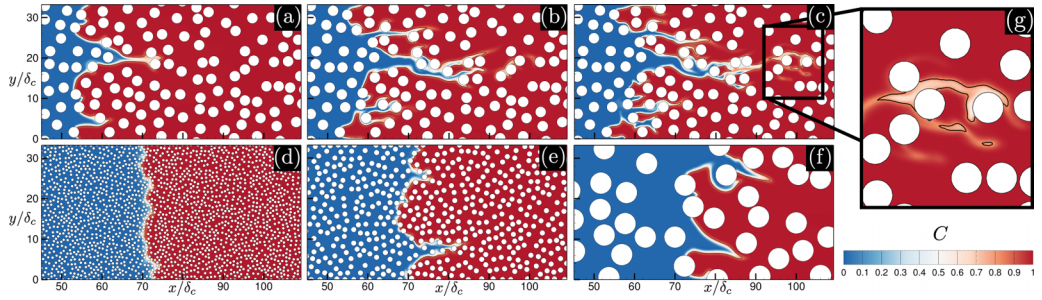

FIG. 1. Instantaneous fields of the reaction progress $C = 1 - Y_F/Y_{F,u}$ defined from the fuel mass fraction Y_F, with $Y_{F,u}$ the value at the inlet (left). The mixture flows from left to right: (a)–(c) at a fixed pore size $D/\delta_c = 2.7$ for different Darcy velocities, (a) $U_D/S_L = 2.5$ ($\mathrm{Re}_p = 82$), (b) $U_D/S_L = 5.6$ ($\mathrm{Re}_p = 183$), (c) $U_D/S_L = 16.4$ ($\mathrm{Re}_p = 539$); and (d)–(f) at comparable Darcy velocities $U_D/S_L = 2.6 \pm 0.2$ for different pore sizes, (d) $D/\delta_c = 0.67$ ($\mathrm{Re}_p = 20$), (e) $D/\delta_c = 1.33$ ($\mathrm{Re}_p = 39$), (f) $D/\delta_c = 5.3$ ($\mathrm{Re}_p = 185$). Panel (g) zooms into disconnected pockets of unreacted gases with $C < 0.85$ in (c). The porous media starts at $x = 0$, and only parts of the simulated domains are shown.

stretching mechanism akin to 3D turbulence, although baroclinic torque and density changes can also impact the 2D vorticity balance near chemical reaction fronts [29]. But the primary source of 2D flow vorticity is through creation, and to a lesser extent destruction, at the solid boundary [35]. The flow vorticity thus injected through the solid corrugates the reaction front, feeds its hydrodynamic instabilities, and results in its close packing within the pores. Figure 1 presents instantaneous contours of reaction progress for different inlet velocities and pore diameters, illustrating this reaction-front packing and the complex flow-chemistry coupling regimes.

Figures 1(a)–1(c) shows that the front corrugation rises with increasing inlet velocity, until disconnected pockets of unreacted mixtures propagate downstream within the reactive mixture [Fig. 1(g)]. In contrast, for a fixed inlet velocity [Fig. 1(d)–1(f)], increasing the pore diameter has a comparatively low impact on the corrugation intensity but leads to the formation of larger eddies, in agreement with the higher Reynolds number. For cases with comparable Reynolds numbers, the unsteady flow only wrinkles the reaction front for large pores [$D/\delta_c = 5.3$ in Fig. 1(f)], whereas smaller pores result in deep and narrow fingers where strong coupling effects emerge [$D/\delta_c = 2.7$ in Fig. 1(b)].

To further examine these differences in flow-chemistry coupling across conditions, we evaluate the chemical reactivity via the global consumption speed S_c defined as $S_c = \int_\Omega \dot{\omega}_F \, \mathrm{d}\Omega/(A_\perp \rho_u Y_{F,u})$ [36], where $\dot{\omega}_F$ is the volumetric rate of fuel mass consumption, $A_\perp$ is the cross-sectional area of the domain, and $\rho_u Y_{F,u}$ is the fuel density in the unreacted mixture [13]. The time average of the consumption speed $\overline{S_c}$ indicates whether the reaction front remains anchored ($U_D = \overline{S_c}$), or whether it propagates upstream ($U_D < \overline{S_c}$) or downstream ($U_D > \overline{S_c}$) of the porous media.

For anchored reaction fronts, the folding of the reaction surface can be directly quantified from the consumption speed by considering a linear surface density model [15,29]. The fuel consumption rate is represented as $\dot{\omega}_F = \rho_u Y_{F,u} S_L \Sigma$, with Σ the flame surface density. The Lewis number is set to unity such that the local reaction speed is independent of stretch, a common assumption for lean methane-air combustion [29,36,37]. Then, by representing the deviation to the surface density model by a term σ_c to account for super-linear chemical consumption, the budget of the instantaneous consumption speed can be written as

$$\frac{S_c}{S_L} = \frac{\int_\Omega S_L \Sigma \, \mathrm{d}\Omega}{S_L A_\perp} + \frac{\sigma_c}{S_L} = \frac{A_f^p}{A_\perp} + \frac{A_f^d}{A_\perp} + \frac{\sigma_c}{S_L}, \tag{1}$$

where A_f^p is the area of the primary reaction front, and A_f^d is the area of disconnected reaction pockets.

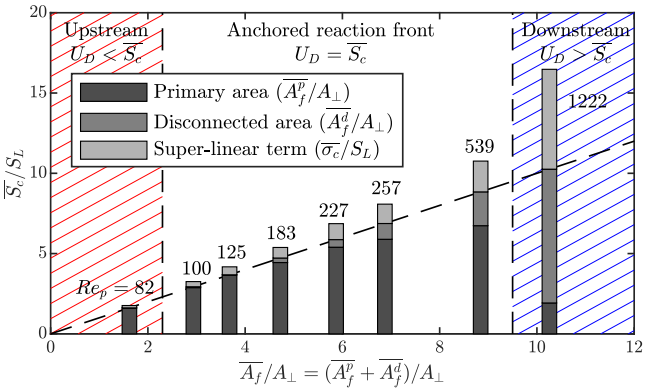

FIG. 2. Time-averages of consumption speed $\overline{S_c}$ and reaction front surface $\overline{A_f}$ for the indicated pore Reynolds number Re_p in an irregular cylinder array with $D/\delta_c = 2.7$. The contributions from the primary reaction front $\overline{A_f^p}$ and disconnected regions $\overline{A_f^d}$ are separated. The dashed line indicates the linear increase in consumption from flamelet corrugation according to $\overline{S_c}/S_L = \overline{A_f}/A_\perp$, and above which the additional term computed as $\overline{\sigma_c}/S_L = \overline{S_c}/S_L - \overline{A_f}/A_\perp$ corresponds to a superlinear chemical consumption.

Figure 2 presents time-averaged budgets of the terms defined in Eq. (1) for the simulations shown in Figs. 1(a)–1(c) with varying inlet velocities. For low corrugation levels, the chemical consumption increases nearly linearly with the flame surface, a characteristic of weak coupling: dispersion wrinkles the reaction zone without affecting its inner structure, and the linear surface density model is valid, because $\overline{\sigma_c}/S_L \ll 1$. This weak coupling regime therefore appears similar to the free-turbulence regime of corrugated reaction fronts, or wrinkled flamelets [38].

In contrast, at high levels of corrugation, the enhancement in chemical reactivity exceeds the relative increase in flame area. The corrugation of the primary reaction front then accounts for only $60 - 70\%$ of the chemical consumption $\overline{S_c}/S_L$, thus deviating from the linear surface density model. In fact, two unsteady physical processes emerge, resulting in a transition to a regime of strong dispersion-chemistry coupling.

First, the separation of pockets of unreacted gases downstream of the primary reaction front starts to contribute significantly to the total flame area, as measured through the disconnected area term A_f^d in Eq. (1). This term increases with increasing inlet velocity, reaching a contribution $\overline{A_f^d}/A_\perp$ of up to 20% of the chemical consumption $\overline{S_c}/S_L$ for anchored reaction fronts. Similar pockets form in pulsating laminar flows [39] and in free turbulence [40,41].

Second, the chemical reactivity intermittently increases far beyond what is predicted by the linear surface density model, especially when reaction pockets separate from the primary reaction front (Fig. S1 in the Supplemental Material [31]). These spikes in consumption rate are due to the formation of elongated fingers where the flow-through time becomes comparable to the characteristic chemical response time (Fig. S2 in the Supplemental Material [31]). The same cusps emerge in unconfined reactive flows with significant turbulence [30].

These results show that dispersion in porous media influences the chemistry through three distinct processes: front corrugation, pocket separation, and cusp formation. The stretch of the reaction front represents a fourth possible coupling process, although it does not impact chemical consumption here given the unity Lewis number. In unconfined 2D and 3D turbulent flows, the same four processes also govern turbulence-chemistry interactions [30,40], thus indicating direct similarities between how free turbulence and hydrodynamic dispersion in porous media impact chemical reaction fronts. We note one major distinction, however: in the 2D flows simulated, dispersion altered the chemistry at steady flow conditions with static reaction fronts, as well as at unsteady laminar flow conditions that resemble unconfined pulsating flows. Our analysis of reaction

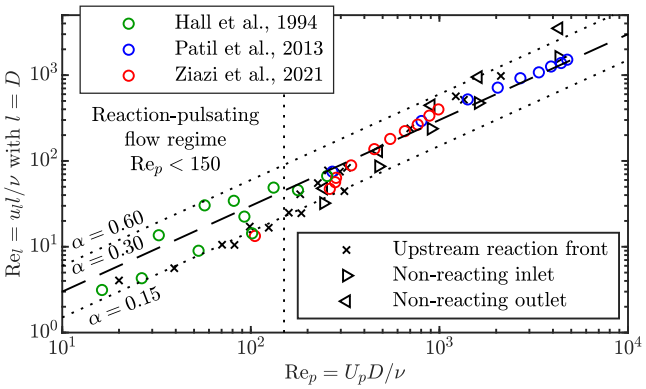

FIG. 3. Spatial mean of the turbulent Reynolds number Re_l at the integral scale as a function of pore-scale Reynolds number Re_p for different inlet velocity, cylinder diameter, and array disorder. The dashed lines indicate the correlation $u_l = \alpha U_p$. For reactive flows, statistics are only acquired upstream of the reaction front. For the nonreactive flows, the statistics are acquired from the first and last 1.6 cm within the porous media. The colored symbols correspond to nonreactive flows reported in the literature [42–44].

front curvature and flow strain also suggests differences in the response to stretching. For non-unity Lewis numbers, the porous media would induce a mean positive stretch from flow strain, such as in turbulent flows, but a mean negative stretch from curvature (see Figs. S3 and S4 in the Supplemental Material [31]), unlike the mean zero distribution observed in free turbulence [37,38].

Impact of chemistry on dispersion. Reciprocally, chemical reaction fronts also alter the pore-scale flow dynamics and inertial regimes. Here, we first identify nominal transition baselines in inert flow simulations: Darcy flows are observed for $\mathrm{Re}_p < 50$, while unsteady flow behavior arises for $\mathrm{Re}_p > 150$ (see Figs. S5 and S6 in the Supplemental Material [31]). Pore-scale turbulence develops for $\mathrm{Re}_p > 300$ [10] and behaves similarly to free isotropic turbulence for $\mathrm{Re}_p > 1300$ [10]. Note that these transition values vary depending upon the porous media 2D or 3D configuration, porosity, and Reynolds number definition.

In our reactive flow simulations, the transition outside the Darcy regime is unchanged upstream of the reaction front ($\mathrm{Re}_p = 50$), despite a more viscous flow downstream with a ratio of dynamic viscosity $\mu_d/\mu_u = 3.45$ [12,29]. But the inherently unstable reaction front triggers an early transition to unsteady flows at Reynolds numbers below $\mathrm{Re}_p = 100$ for anchored reaction fronts, and as low as $\mathrm{Re}_p = 20$ for upstream propagating fronts, well below the nominal $\mathrm{Re}_p = 150$ transition. We refer to this regime as the pulsating reaction regime, since the unsteady reaction front feeds velocity fluctuations despite remaining anchored on average.

At higher Reynolds numbers, the flow becomes increasingly unsteady. To quantify this increase, we evaluate the integral velocity fluctuations $u_l = \sqrt{k}$ from the turbulence kinetic energy $k = \overline{(\mathbf{u}')^2}/2$, where $\overline{(\mathbf{u}')^2}$ is the time variance of the flow velocity averaged over the pore space. For this calculation, the statistics of the velocity field $\mathbf{u}$ are acquired upstream ($C < 0.02$) and downstream ($C > 0.98$) of the reaction front for the flow region within the pores. In the reaction front brush, the statistics are weighted with the duration over which $C < 0.02$ or $C > 0.98$.

In unsteady inert flows, the intuitive scaling $u_l = \alpha U_p$ with α constant is supported by velocimetry measurements [42–44]. With $\alpha = 0.3$, the results shown in Fig. 3 confirm that both literature measurements and our inert simulations are valid within a factor of two over an entire range of flow conditions, from $\mathrm{Re}_p = 15$ to $\mathrm{Re}_p = 5000$. Furthermore, previous 3D simulations indicate that the same scaling also holds for reactive flow conditions, with u_l measured upstream of the reaction front [8,11]. Here, we evaluate this hypothesis over a wide range of reactive flow conditions. Figure 3

shows that $u_l \approx 0.3U_p$ indeed holds across regimes: from laminar pulsating reaction flows with $\mathrm{Re}_p = 20$ to significantly more unsteady flows with $\mathrm{Re}_p = 2120$.

These results suggest that the turbulence kinetic energy added to the flow by the unsteady dynamics of the reaction front compensates for the higher viscosity downstream of the reaction front. Overall, the pore-scale interactions between dispersion and chemistry remain predominantly one-way coupled, where the prevailing impact of dispersion onto the pore-scale chemistry resembles the impact of turbulence in unconfined flows. The flow notably transitions to a strong coupling regime in which hydrodynamic dispersion significantly alters the reaction front.

A criterion for strong pore-scale coupling. In unconfined turbulent flows, strong turbulence-chemistry interaction is defined for $\mathrm{Ka} > 1$ [45,46], with cusps forming for $\mathrm{Ka} > 20$ in 3D [30]. For homogeneous and isotropic 3D turbulence, the Kolmogorov cascade governs the energy transfer to the viscous scale characterized by time-scale τ_K, velocity-scale u_K, and length-scale l_K ($u_K l_K/\nu = 1$). From the 5/3 rate of the Kolmogorov energy cascade, the Karlovitz number is commonly evaluated from integral-scale flow properties as $\mathrm{Ka} = \tau_c/\tau_K = (u_l/S_L)^{3/2}(\delta_f/l)^{1/2}$. This expression is fundamental to our understanding of turbulence-chemistry interaction, and the differences among the regimes of corrugated flamelet, thin reaction zone, and broken reaction zone [45,46].

In porous media flows, turbulence features integral eddies that scale with the pore size $l = D$ over wide ranges of Reynolds numbers, as evidenced by the unity Strouhal number characterizing vortex-shedding in tube bundles [47]. This scaling is due to the no-slip wall condition that prevents turbulent kinetic energy transport across pores [48–50] and the introduction of velocity fluctuations at the characteristic pore-length scale through hydrodynamic dispersion. In the limit of high Reynolds number ($\mathrm{Re}_p > 1300$), pore-scale 3D turbulence asymptotically resembles 3D turbulence in unconfined flows [49,50]. The $\mathrm{Ka} > 1$ criterion for strong coupling is therefore likely to remain valid. However, in the transitional regime ($\mathrm{Re}_p < 300$) the turbulence cascade is not yet activated, and eddies are as large as the pores. Therefore, from these considerations, we propose that strong pore-scale coupling in the transitional flow regime is determined by the theoretical criterion $\tau_c > \tau_l = l/u_l$, that is $\mathrm{Da} < 1$.

In the 2D flows simulated, there is no vortex stretching, and the turbulence times at the viscous and integral scales remain equal independently of Reynolds numbers. As such, $\mathrm{Ka} > 1$ and $\mathrm{Da} < 1$ are equivalent (see Eq. (S4) in the Supplemental Material [31]). In contrast, there is vortex-stretching in 3D and, as the Kolmogorov cascade establishes with increasing Reynolds number, 3D turbulence resembles that of a channel flow with viscous boundary layers [50]. This suggests that the theoretical 3D criterion denoting strong turbulence-chemistry interaction asymptotically converges from $\mathrm{Da} < 1$ to $\mathrm{Ka} > 1$ as turbulence develops.

Regime diagrams of flow-chemistry coupling. We develop the regime diagram shown in Fig. 4 to simultaneously describe the unsteady flow regimes and the flow-chemistry coupling at the pore scale using chemical, flow, and pore-length scales. On this diagram, constant values for the pore-scale Reynolds number Re_p, the turbulent Reynolds number Re_l, the Damköhler number Da, and the Karlovitz number Ka correspond to diagonal lines that delineate the flow regimes (see Eqs. (S5)–(S8) in the Supplemental Material [31]).

The flows simulated in this work are indicated in Fig. 4, where $\mathrm{Ka} = 1/\mathrm{Da}$ given the 2D nature of the flows considered and the fundamental difference between 2D and 3D turbulence. Even though there is no vortex stretching in 2D, significant amounts of flow vorticity are injected at the solid boundaries in the flows simulated. Thus, unlike in unconfined 2D reactive flows for which chemistry-generated turbulence is the only source of vorticity creation [29], reactive flows in porous media feature, even in 2D, complex unsteady dynamics characterized by vorticity creation and destruction. To consider the implications of this work for 3D conditions, a separate Karlovitz line defined from the 3D Kolmogorov cascade is added in Fig. 4, although future work is required to validate these implications.

For the 2D flows simulated here, the diagram in Fig. 4 shows that all cases featuring superlinear chemical consumption fall within the $\mathrm{Da} < 1.3$ region, which is reasonably consistent with the

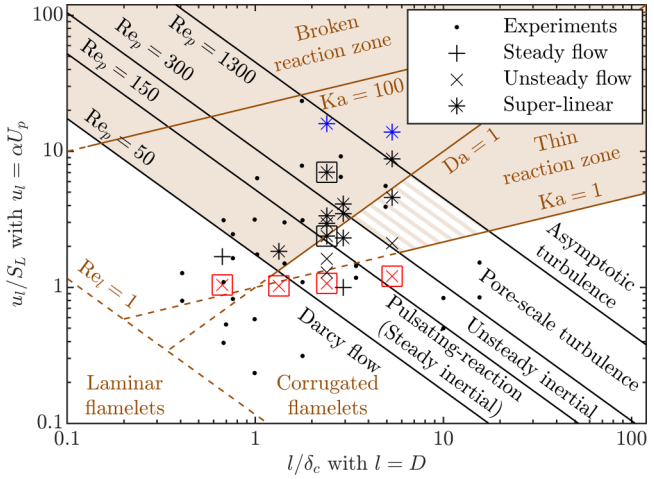

FIG. 4. Regime diagram of reactive flows in porous media populated with the flow conditions simulated in this study and those examined in literature experiments (black dots, see Fig. S7 in the Supplemental Material [31]). Regions of strong dispersion-chemistry coupling are indicated with brown shadings. The Reynolds transition values are obtained from nonreactive simulations, and the lines shown are for $\alpha = 0.3$, $\nu = 1.6 \times 10^{-5}$ m^2/s, $S_L = 23$ cm/s, and $\delta_c = 0.6$ mm. The colored symbols indicate simulations with reaction fronts propagating upstream (in red, $U_D < \overline{S_c}$), or downstream (in blue, $U_D > \overline{S_c}$). Cases for which $\overline{S_c}/S_L > 1.15\overline{A_f}/A_\perp$ are denoted as superlinear. The symbols enclosed in squares correspond to the cases shown in Fig. 1. The locations of symbols are offset by up to 10% for readability.

proposed criterion. In addition, since strong coupling is activated by unsteady hydrodynamics, we expect only weak coupling at steady flow conditions. This hypothesis is confirmed by the steady reactive flow at $\mathrm{Re}_p = 32$ and with a linear chemical response, despite a low Damköhler number ($\mathrm{Da} = 0.4$). Therefore, the transition between weak and strong regimes of dispersion-chemistry interaction is delineated by the line $\mathrm{Re}_p \approx 50$ marking the transition between steady and unsteady pulsating reaction flows with anchored fronts, and by the lines of unity Damköhler and Karlovitz numbers, indicating whether or not the reaction front structure is altered by flow perturbations. The simulations also support that anchored reaction fronts transition to upstream propagation when $\alpha U_p/S_L < 1$, confirming that the critical anchoring velocity is relatively independent of pore size [25].

To visualize the regime distribution relevant to practical applications, the flow conditions examined in 11 experimental studies from the literature are also indicated in Fig. 4, based on the scaling laws $l = D$ and $u_l = \alpha U_p$ (see Fig. S7 in the Supplemental Material [31]). This diagram shows that practical flow conditions can cover widely different regimes, for instance, for significantly larger pore sizes [6,16], or high-pressure conditions with chemical length scales changing by a factor of six [6,11,51]. Yet, most practical applications fall between the laminar steady and transitional flow regimes near $\mathrm{Da} \approx 1$ and are thus likely to feature a regime transition in the dispersion-chemistry coupling.

Porosity can also vary widely, from 0.1 in geological flows to 0.9 in reticulated foams, whereas in this paper it is kept constant at 0.7. A systematic study of the role of porosity and porous media connectivity is beyond the scope of this paper, but the theory developed can provide some insights for discussion. First, the interstitial velocity and Reynolds number definition used in the regime diagram are dependent on porosity. Reducing the porosity at constant Darcy flux thus increases the interstitial velocity fluctuations, which could trigger a regime transition. Second, the constant α and the Reynolds transition values from this paper are likely to depend on porosity, such that alternative Reynolds number definitions may prove more adequate depending on the application

[21]. Furthermore, at low porosity values, the pore size becomes only a fraction of the solid grain size. In this case, regime predictions may be more reliable by relating the turbulence-integral length-scale to the pore size, instead of the characteristic solid size as done in this paper.

Conclusions. This article presents a theoretical framework to understand reactive flows in porous media. Simulation results indicate that pore-scale dispersion and unsteady hydrodynamics can, even at laminar pore-scale flow conditions, impact the flow-chemistry interaction to an extent comparable to unconfined turbulence. A diagram is thus developed to evaluate the pore-scale coupling regimes from direct parameters of the chemistry, flow, and porous media. In particular, this paper shows that $\mathrm{Da} < 1$ is a required condition for strong coupling in 2D flows, while in 3D flows, the proposed theory suggests that only the weaker condition $\mathrm{Ka} > 1$ is necessary. Because the complexity of reactive flows in porous media stems from the regime-dependent nature of the underlying physical processes, this regime diagram could become instrumental in our understanding of these flows and relevant to a broad range of applications.

Acknowledgments. This work was supported by a Leading Edge Aeronautics Research for NASA (LEARN) Grant (No. NNX15AE42A) and by the National Science Foundation (Award No. CBET-1800906 and Graduate Research Fellowship with No. 1656518). Fruitful discussions with Alexei Poludnenko are gratefully acknowledged.

[1] C. Li, S. M. Meckler, Z. P. Smith, J. E. Bachman, L. Maserati, J. R. Long, and B. A. Helms, Engineered transport in microporous materials and membranes for clean energy technologies, Adv. Mater. **30**, 1704953 (2018).

[2] H. Khodaei, Y. M. Al-Abdeli, F. Guzzomi, and G. H. Yeoh, An overview of processes and considerations in the modelling of fixed-bed biomass combustion, Energy **88**, 946 (2015).

[3] K. A. Al-attab, J. C. Ho, and Z. A. Zainal, Experimental investigation of submerged flame in packed bed porous media burner fueled by low heating value producer gas, Exp. Therm Fluid Sci. **62**, 1 (2015).

[4] Q. Li, J. Li, J. Shi, and Z. Guo, Effects of heat transfer on flame stability limits in a planar micro-combustor partially filled with porous medium, Proc. Combust. Inst. **37**, 5645 (2019).

[5] F. Sirotkin, R. Fursenko, S. Kumar, and S. Minaev, Flame anchoring regime of filtrational gas combustion: Theory and experiment, Proc. Combust. Inst. **36**, 4383 (2017).

[6] Z. Chen, J. Shi, M. Xie, and M. Yue, A numerical investigation on the rapid turbulent filtration combustion under high background pressure, Combust. Sci. Technol. **194**, 3039 (2022).

[7] N. Djordjevic, P. Habisreuther, and N. Zarzalis, A numerical investigation of the flame stability in porous burners employing various ceramic sponge-like structures, Chem. Eng. Sci. **66**, 682 (2011).

[8] I. Yakovlev and S. Zambalov, Three-dimensional pore-scale numerical simulation of methane-air combustion in inert porous media under the conditions of upstream and downstream combustion wave propagation through the media, Combust. Flame **209**, 74 (2019).

[9] M. Sahimi, *Flow and Transport in Porous Media and Fractured Rock: From Classical Methods to Modern Approaches*, 2nd ed. (Wiley-VCH, Weinheim, 2011).

[10] B. D. Wood, X. He, and S. V. Apte, Modeling turbulent flows in porous media, Annu. Rev. Fluid Mech. **52**, 171 (2020).

[11] C. Bedoya, I. Dinkov, P. Habisreuther, N. Zarzalis, H. Bockhorn, and P. Parthasarathy, Experimental study, 1D volume-averaged calculations and 3D direct pore level simulations of the flame stabilization in porous inert media at elevated pressure, Combust. Flame **162**, 3740 (2015).

[12] N. F. Jouybari, M. Maerefat, and M. E. Nimvari, A pore scale study on turbulent combustion in porous media, Heat Mass Transfer **52**, 269 (2016).

[13] J. C. Ferguson, S. Sobhani, and M. Ihme, Pore-resolved simulations of porous media combustion with conjugate heat transfer, Proc. Combust. Inst. **38**, 2127 (2021).

[14] R. Borghi, On the structure and morphology of turbulent premixed flames, in *Recent Adv. Aerosp. Sci.* (Springer, Boston, MA, 1985), pp. 117–138.
[15] J. F. Driscoll, Turbulent premixed combustion: Flamelet structure and its effect on turbulent burning velocities, Prog. Energy Combust. Sci. **34**, 91 (2008).
[16] R. V. Fursenko, I. A. Yakovlev, E. S. Odintsov, S. D. Zambalov, and S. S. Minaev, Pore-scale flame dynamics in a one-layer porous burner, Combust. Flame **235**, 111711 (2022).
[17] I. Yakovlev, A. Maznoy, and S. Zambalov, Pore-cale study of complex flame stabilization phenomena in thin-layered radial porous burner, Combust. Flame **231**, 111468 (2021).
[18] K. Dobrego and A. Chornyi, Parallels between the regimes of turbulent and filtration combustion of gases in inert porous media, J. Eng. Phys. Thermophys **74**, 581 (2001).
[19] L. Chen, Q. Kang, Y. L. He, and W. Q. Tao, Pore-scale simulation of coupled multiple physicochemical thermal processes in micro reactor for hydrogen production using lattice Boltzmann method, Int. J. Hydrogen Energy **37**, 13943 (2012).
[20] R. C. Rocha, C. F. Ramos, M. Costa, and X. S. Bai, Combustion of NH_3/CH_4/Air and NH_3/H_2/Air mixtures in a porous burner: Experiments and kinetic modeling, Energy Fuels **33**, 12767 (2019).
[21] S. Arbabi and M. Sahimi, The transition from Darcy to nonlinear flow in heterogeneous porous media: I—Single-phase flow, Transp. Porous Media **151**, 795 (2024).
[22] K. Alim, S. Parsa, D. A. Weitz, and M. P. Brenner, Local pore size correlations determine flow distributions in porous media, Phys. Rev. Lett. **119**, 144501 (2017).
[23] K. V. Dobrego, S. A. Zhdanok, and A. I. Zaruba, Experimental and analytical investigation of the gas filtration combustion inclination instability, Int. J. Heat Mass Transf. **44**, 2127 (2001).
[24] C. Wieland, C. Weis, P. Habisreuther, and D. Trimis, 3D direct pore level simulations of radiant porous burners, Combust. Flame **245**, 112370 (2022).
[25] I. Yakovlev, D. Astakhov, S. Zambalov, R. Fursenko, J. Li, and A. Maznoy, Transition to unstable oscillatory flames in porous media combustion, Combust. Flame **252**, 112752 (2023).
[26] P. A. Masset, F. Duchaine, A. Pestre, and L. Selle, Modelling challenges of volume-averaged combustion in inert porous media, Combust. Flame **251**, 112678 (2023).
[27] E. Boigné, T. Zirwes, D. Parkinson, G. Vignat, P. Muhunthan, H. Barnard, A. MacDowell, and M. Ihme, Integrated experimental and computational analysis of porous media combustion by combining gas-phase synchrotron μCT, IR-imaging, and pore-resolved simulations, Combust. Flame **259**, 113132 (2024).
[28] R. J. Kee, M. E. Coltrin, P. Glarborg, and H. Zhu, *Chemically Reactive Flow: Theory and Practice*, 2nd ed. (John Wiley & Sons, Hoboken, NJ, 2017).
[29] T. Poinsot and D. Veynante, *Theoretical and Numerical Combustion*, 2nd ed. (R.T. Edwards, Philadelphia, PA, 2005).
[30] A. Y. Poludnenko and E. S. Oran, The interaction of high-speed turbulence with flames: Turbulent flame speed, Combust. Flame **158**, 301 (2011).
[31] See Supplemental Material at http://link.aps.org/supplemental/10.1103/PhysRevFluids.9.L101201 for simulation details, supporting analysis, and construction of regime diagram.
[32] P. C. Ma, Y. Lv, and M. Ihme, An entropy-stable hybrid scheme for simulations of transcritical real-fluid flows, J. Comput. Phys. **340**, 330 (2017).
[33] Q. Douasbin, M. Ihme, and C. Arndt, Pareto-efficient combustion framework for predicting transient ignition dynamics in turbulent flames: Application to a pulsed jet-in-hot-coflow flame, Combust. Flame **223**, 153 (2021).
[34] P. de Anna, B. Quaife, G. Biros, and R. Juanes, Prediction of the low-velocity distribution from the pore structure in simple porous media, Phys. Rev. Fluids **2**, 124103 (2017).
[35] B. R. Morton, The generation and decay of vorticity, Geophys. Astrophys. Fluid Dyn. **28**, 277 (1984).
[36] J. B. Bell, R. K. Cheng, M. S. Day, and I. G. Shepherd, Numerical simulation of Lewis number effects on lean premixed turbulent flames, Proc. Combust. Inst. **31**, 1309 (2007).
[37] D. C. Haworth and T. J. Poinsot, Numerical simulations of Lewis number effects in turbulent premixed flames, J. Fluid Mech. **244**, 405 (1992).
[38] N. Chakraborty, M. Klein, and R. S. Cant, Stretch rate effects on displacement speed in turbulent premixed flame kernels in the thin reaction zones regime, Proc. Combust. Inst. **31**, 1385 (2007).

[39] M. Talei, E. R. Hawkes, and M. J. Brear, A direct numerical simulation study of frequency and Lewis number effects on sound generation by two-dimensional forced laminar premixed flames, Proc. Combust. Inst. **34**, 1093 (2013).

[40] J. H. Chen, T. Echekki, and W. Kollmann, The mechanism of two-dimensional pocket formation in lean premixed methane-air flames with implications to turbulent combustion, Combust. Flame **116**, 15 (1999).

[41] R. A. Griffiths, J. H. Chen, H. Kolla, R. S. Cant, and W. Kollmann, Three-dimensional topology of turbulent premixed flame interaction, Proc. Combust. Inst. **35**, 1341 (2015).

[42] M. J. Hall and J. P. Hiatt, Exit flows from highly porous media, Phys. Fluids **6**, 469 (1994).

[43] V. A. Patil and J. A. Liburdy, Turbulent flow characteristics in a randomly packed porous bed based on particle image velocimetry measurements, Phys. Fluids **25**, 043304 (2013).

[44] R. M. Ziazi and J. A. Liburdy, Vortical structures and mixing characteristics of flow in randomly packed porous media during transition to turbulence, in *Fluids Eng. Div. Summer Meet.*, Vol. 85307 (ASME, 2021), V003T05A025.

[45] N. Peters, Laminar flamelet concepts in turbulent combustion, Symp. (Int.) Combust. **21**, 1231 (1988).

[46] F. Williams, Turbulent combustion, in *The Mathematics of Combustion* (SIAM, Philadelphia, PA, 1985), pp. 97–131.

[47] D. S. Weaver, J. A. Fitzpatrick, and M. Elkashlan, Strouhal numbers for heat exchanger tube arrays in cross flow, J. Pressure Vessel Technol. **109**, 219 (1987).

[48] I. Lim and R. D. Matthews, Development of a model for turbulent combustion within porous inert media, Int. J. Fluid Mech. Res. **25**, 111 (1998).

[49] M. F. Uth, Y. Jin, A. V. Kuznetsov, and H. Herwig, A direct numerical simulation study on the possibility of macroscopic turbulence in porous media: Effects of different solid matrix geometries, solid boundaries, and two porosity scales, Phys. Fluids **28**, 065101 (2016).

[50] Y. Jin and A. V. Kuznetsov, Turbulence modeling for flows in wall bounded porous media: An analysis based on direct numerical simulations, Phys. Fluids **29**, 045102 (2017).

[51] S. Sobhani, J. Legg, D. F. Bartz, J. J. Kojima, C. T. Chang, J. D. Sullivan, J. P. Moder, and M. Ihme, Experimental investigation of lean premixed pre-vaporized liquid-fuel combustion in porous media burners at elevated pressures up to 20 bar, Combust. Flame **212**, 123 (2020).